Anode Catalysts in Anion-Exchange-Membrane

Electrolysis Without Supporting Electrolyte:

Conductivity, Dynamics, and Ionomer Degradation

Raina A. Krivina and Grace A. Lindquist, Sarah R. Beaudoin, T. Nathan Stovall, Willow L.

Thompson, Liam P. Twight, Douglas Marsh, Joseph Grzyb, Kevin Fabrizio, James E. Hutchison,

and Shannon W. Boettcher \*

R. A. Krivina, G. A. Lindquist, S. R. Beaudoin, T. N. Stovall, W. L. Thompson, Liam P. Twight,

Douglas Marsh, Joseph Grzyb, S. W. Boettcher

Department of Chemistry and Biochemistry and the Oregon Center for Electrochemistry

University of Oregon

Eugene, Oregon 97403, USA

E-mail: swb@uoregon.edu

K. Fabrizio, J. E. Hutchison

Department of Chemistry and Biochemistry, University of Oregon

Eugene, Oregon 97403, USA

Keywords: anion-exchange membrane, membrane electrolysis, alkaline water electrolysis,

oxygen evolution catalysis, non-platinum-group-metal catalyst.

1

Anion-exchange-membrane water electrolyzers (AEMWEs) in principle operate without soluble electrolyte using earth-abundant catalysts and cell materials and thus lower the cost of green H<sub>2</sub>. Current systems lack competitive performance and durability needed for commercialization. One critical issue is a poor understanding of catalyst-specific degradation processes in the electrolyzer. While non-platinum-group-metal (non-PGM) oxygen-evolution catalysts show excellent performance and durability in strongly alkaline electrolyte, this has not transferred directly to purewater AEMWEs. Here, AEMWEs with five non-PGM anode catalysts are built and the catalysts' structural stability and interactions with the alkaline ionomer are characterized during electrolyzer operation and post-mortem. The results show catalyst electrical conductivity is one key to obtaining high-performing systems and that many non-PGM catalysts restructure during operation. Dynamic Fe sites correlate with enhanced degradation rates, as does the addition of soluble Fe impurities. In contrast, electronically conductive Co<sub>3</sub>O<sub>4</sub> nanoparticles (without Fe in the crystal structure) yield AEMWEs from simple, standard preparation methods, with performance and stability comparable to IrO<sub>2</sub>. These results reveal the fundamental dynamic catalytic processes resulting in AEMWE device failure under relevant conditions, demonstrate a viable non-PGM catalysts for AEMWE, and illustrate underlying design rules for engineering anode catalyst/ionomer layers with higher performance and durability.

#### 1. Introduction

Water electrolysis powered by renewable energy produces green H<sub>2</sub> fuel, which is central for a 100% renewable energy economy. <sup>[1, 2]</sup> Of the low-temperature water-electrolysis technologies, alkaline water electrolysis (AWE) is the most mature. AWE operates in hot, liquid-alkaline electrolyte (~80 °C, ~5 M KOH) with two electrodes separated by a porous diaphragm. It provides high efficiency and uses earth-abundant non-platinum-group-metal (non-PGM) materials, but is affected in performance and capital expense due to gas crossover through the porous separator and shunt currents through the electrolyte flow paths. <sup>[3, 4]</sup> Proton-exchange-membrane (PEM) electrolyzers use a thin (~20-50 μm) cation-selective solid-ionomer membrane that reduces gas crossover, enables operation at higher currents (> 2 A cm<sup>-2</sup>), and eliminates shunt currents with a pure-water feed. <sup>[5]</sup> However, the locally-acidic environment created by the PEM requires expensive PGM catalysts. Anion-exchange-membrane (AEM) electrolysis is a developing technology that combines the benefits of AWE and PEM, ideally operating in water with no supporting liquid electrolyte under differential pressure and providing a locally-alkaline environment for non-PGM catalysts and materials. <sup>[4]</sup>

To date, AEM water electrolyzers (AEMWEs) do not have comparable performance or durability to PEM or AWE systems. <sup>[3, 5]</sup> To compensate, most AEMWEs use soluble supporting electrolyte, commonly carbonate or hydroxide, to improve conductivity and increase apparent durability. <sup>[6-11]</sup> The use of supporting electrolyte, however, has practical implications that complicate system design as discussed above and masks underlying degradation phenomena that are important to prevent. <sup>[12]</sup> Understanding the factors that control performance and durability in the absence of supporting electrolyte is therefore an important immediate goal.

Most AEMWE testing is conducted with expensive IrO<sub>2</sub> oxygen evolution reaction (OER) catalyst because it is stable and active. [13-15] In alkaline electrolyte, however, Ni-Fe oxyhydroxides have the lowest overpotential and highest per-cation turnover frequency in three-electrode studies. [16-18] The performance and durability of Ni-Fe oxyhydroxides has generally been poor in purewater membrane-electrode-assembly (MEA) configurations, however, which we have attributed to difficulties in oxidizing the bulk of the catalyst to its active state without soluble electrolyte. [15] Recently, non-PGM catalysts have shown more-promising performance and durability in MEA configurations, but appear to require either supporting electrolyte [8, 19, 20] or complex electrode and/or catalyst design and preparation, [21] for example with the Ni/Fe catalyst supported on a highsurface-area Ni foam, that may not be easily translated to commercial-scale devices. [10, 22-25] These studies are often further complicated by membrane and ionomer instability that causes degradation independent of catalyst identity. Very few studies have investigated the catalyst-level phenomenon that modulate apparent durability, especially in industry-relevant MEA conditions. Recent developments in AEM ionomer and MEA preparation and assembly have improved AEMWE durability, [13, 14, 22] making it possible to better isolate the role of metal-oxide catalysts in system degradation.

Here, we study five Ni-, Co-, and Fe-oxide-based nanoparticle anode catalysts and compare them to commercial nanoparticle IrO<sub>2</sub> in pure-water AEMWE to understand the fundamental factors controlling the performance and durability of non-PGM materials in industry relevant designs. Using *operando* analysis and post-operation materials characterization, particularly by x-ray photoelectron spectroscopy (XPS) of the catalyst layer, we observe multiple processes contributing simultaneously to degradation. We show differences in structure dynamics of the anode catalysts driven via operation and how catalyst restructuring processes affect the device

performance. We find that the introduction of soluble Fe species during device operation accelerates degradation. Finally, we demonstrate a device using a Co<sub>3</sub>O<sub>4</sub> anode with comparable performance and durability to IrO<sub>2</sub>, proving a viable route for non-PGM operation at scales where IrO<sub>2</sub> may not be viable due to scarcity.

#### 2. Results and Discussion

# 2.1. AEMWE performance and durability

AEMWE devices were constructed for each catalyst following published procedures <sup>[13]</sup> (see Experimental section). Catalysts were dispersed in an ink of isopropyl alcohol, water, and ionomer and sprayed onto gas-diffusion-layer (GDL) substrates. Commercial nanopowders (IrO<sub>2</sub>, Co<sub>3</sub>O<sub>4</sub>, NiO, NiCoO<sub>2</sub>, NiFe<sub>2</sub>O<sub>4</sub>, and Ni<sub>0.5</sub>Co<sub>0.5</sub>Fe<sub>2</sub>O<sub>4</sub>) were used as anode catalysts (Table 1) and Pt black as the cathode catalyst.

Table 1: Anode catalyst properties.

Catalyst	Diameter [nm]	Surface Area [m <sup>2</sup> ·g <sup>-1</sup> ]	σ [mS·cm <sup>-1</sup> ]
IrO <sub>2</sub>	5-10	$14.1 \pm 0.1$	metallic*
Co <sub>3</sub> O <sub>4</sub>	30-50	$28.0 \pm 0.1$	$30 \pm 6$
NiO	15-35	$32.4\pm0.1$	$4\pm3$
NiCoO <sub>2</sub>	20	$19.5 \pm 0.1$	$0.9 \pm 0.4$
Ni <sub>0.5</sub> Co <sub>0.5</sub> Fe <sub>2</sub> O <sub>4</sub>	40	$57.7 \pm 0.3$	$0.004 \pm 0.005$
NiFe <sub>2</sub> O <sub>4</sub>	20	$69.6 \pm 0.5$	$0.02 \pm\ 0.01$

<sup>\*</sup>measurement indistinguishable from contact resistance

Anode catalysts were sprayed onto a stainless-steel woven mesh and cathode catalysts on Toray-090 carbon paper. The loading for all catalysts was between 2.2 and 2.7 mg·cm<sup>-2</sup> with 10% by weight ionomer content. A thin layer (2 - 5 wt. % relative to catalyst loading) of ionomer was

sprayed on top of the catalyst layer. The MEAs were constructed using a 40-μm-thick PiperION TP-85 membrane and compressed with a torque on the assembly bolts of 5.6 N·m. Water (at 60 °C ) was pumped to the anode and cathode at 125 mL·min<sup>-1</sup> until the hardware temperature equilibrated to 57 °C. The cell was conditioned prior to data collection as described in the Experimental section. Figure S1 shows a photo of the electrolyzer system and a schematic of the MEA components.

First, the performance and durability of each catalyst was assessed during pure-water electrolyzer operation. IrO<sub>2</sub> out-performed all other catalysts by ~ 100 mV at 10 mA·cm<sup>-2</sup> (Figure 1a). At such a low current density, ohmic and mass-transport losses should be minimal, and performance is largely dominated by the OER overpotential. As current density increases the performance more closely compares to the next-best catalysts, Co<sub>3</sub>O<sub>4</sub> and NiO, which are within 50 mV of IrO<sub>2</sub> at 1 A·cm<sup>-2</sup>. All tested mixed-metal catalysts displayed worse performance. To investigate the origin of this trend, galvanostatic electrochemical impedance spectroscopy (GEIS) was conducted at 50 mA·cm<sup>-2</sup> immediately after cell conditioning (Figure 1b). The data was fit to a Randle's circuit with constant phase elements (Figure 1b inset). All cells show comparable highfrequency series-resistance, and thus the performance discrepancies are not attributed to differences in materials/cell assembly conditions, for example, contact between the catalyst layer and membrane or in the ink dispersion quality. The trend in low-frequency resistance, assigned to charge-transfer phenomena, agrees with the voltage trend observed at 50 mA·cm<sup>-2</sup>, as expected. IrO<sub>2</sub> and Co<sub>3</sub>O<sub>4</sub> also showed the best durability over 20 h, stabilizing to a degradation rate of 2.6 mV·h<sup>-1</sup>and 1.8 mV·h<sup>-1</sup>, respectively (Figure 1c). While NiO showed similar performance, an initial rapid degradation was observed before the electrolyzer stabilized to a degradation rate of 6.4 mV·h<sup>-</sup> <sup>1</sup> at ~200 mV higher voltage than IrO<sub>2</sub> and Co<sub>3</sub>O<sub>4</sub>. Fe-containing catalysts showed exceptionally

high degradation rates, with NiFe<sub>2</sub>O<sub>4</sub> surpassing 5 V after only ~4 h. Although Ni-Fe-oxide-based catalysts substantially outperform IrO<sub>2</sub> in alkaline three-electrode-cell tests, <sup>[16, 18]</sup> in a pure-water-fed MEA with an alkaline catalyst/ionomer environment, the trend in performance appears reversed.

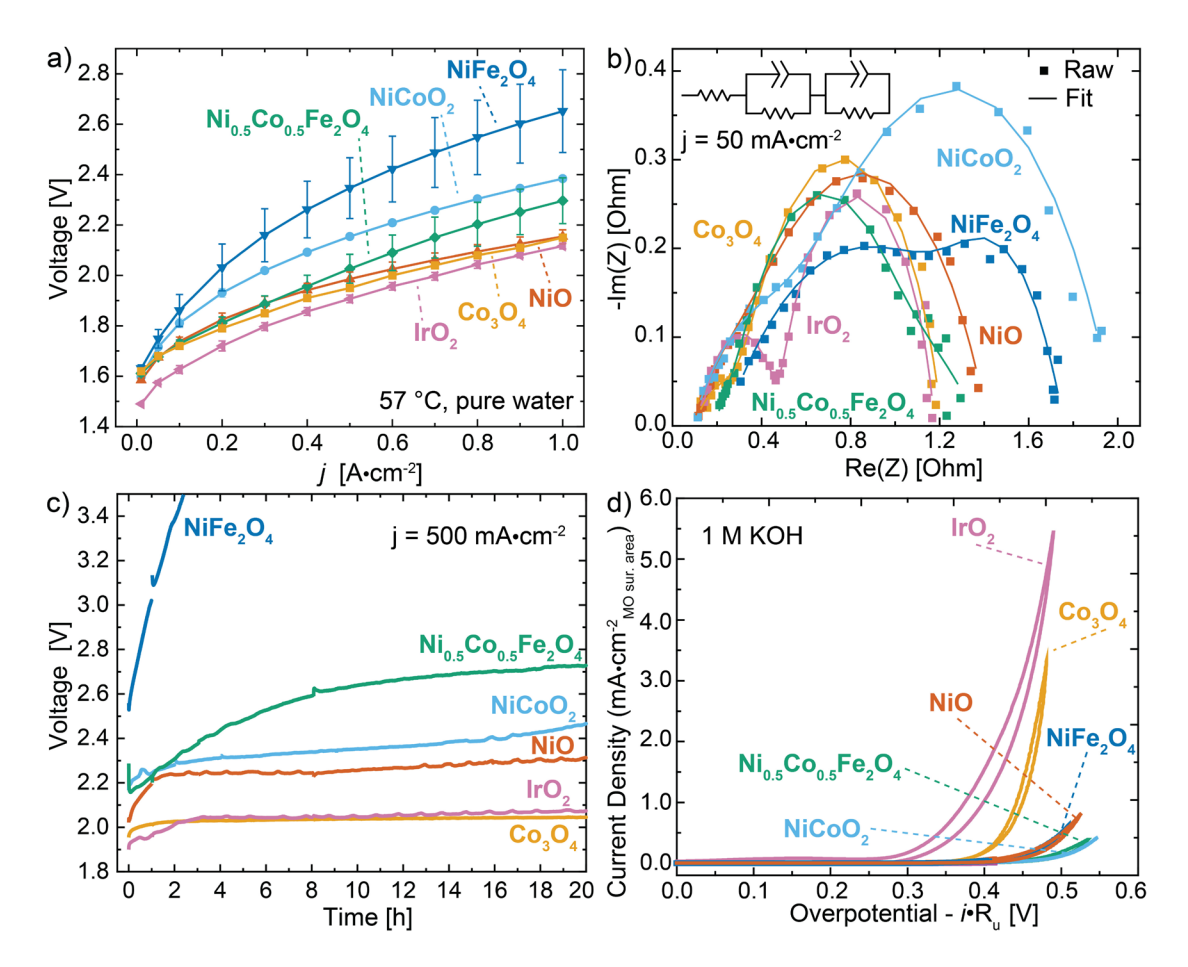


**Figure 1: Electrochemical performance.** a) Polarization curves of anode catalysts tested. All experiments were conducted in pure water at 57 °C. A stainless-steel woven substrate with the indicated catalyst was used as the anode GDL and Pt black catalyst on Toray carbon paper was used as the cathode GDL. Data with iR correction is included in Figure S3. Sample size n = 3; data presented as mean  $\pm$  one standard deviation. b) Galvanostatic electrochemical impedance spectroscopy (GEIS, at 50 mA·cm<sup>-2</sup>) for each catalyst tested in the pure-water MEA for a single representative device. The inset shows the equivalent circuit used for data fitting. c) Durability testing for each catalyst held at 500 mA·cm<sup>-2</sup> for 20 h at 57 °C for a single representative device. Duplicate MEAs are included in Figure S4. d) Cyclic voltammetry for catalysts embedded in anion-

exchange ionomer (10 wt. %) tested in 1.0 M KOH on Au/Ti quartz-crystal-microbalance electrodes. The current density is calculated using the BET surface areas of the nanopowders. The overpotential was corrected for  $R_u$  (3.0 – 3.6  $\Omega$ ). The first CV cycle for one representative electrode is shown for clarity; replicate measurements with additional cycling are shown in Figure S5 and S6.

We tested the same inks used to coat GDLs (catalyst inks with 10 wt. % ionomer) on quartz-crystal electrodes in 1.0 m KOH (Figure 1d) to identify differences between MEA and soluble electrolyte environments for catalysis. IrO<sub>2</sub> and Co<sub>3</sub>O<sub>4</sub> still outperform the Ni/Fe-oxide catalysts. In our previous studies we used less-crystalline Ni/Fe-oxide thin films that converted to the 3<sup>+</sup>/4<sup>+</sup> oxyhydroxide state rapidly during operation, leading to dramatically increased activity. [16, 18] The Ni/Fe nanopowdered oxide catalysts used for the MEA configuration might not easily convert to the more-active oxyhydroxide phase due to low electronic conductivity and, in the MEA, lack of soluble electrolyte that can penetrate the layered structure. Thus, the activity trend observed in prior thin-film studies cannot be directly translated to an ionomer environment in an MEA configuration.

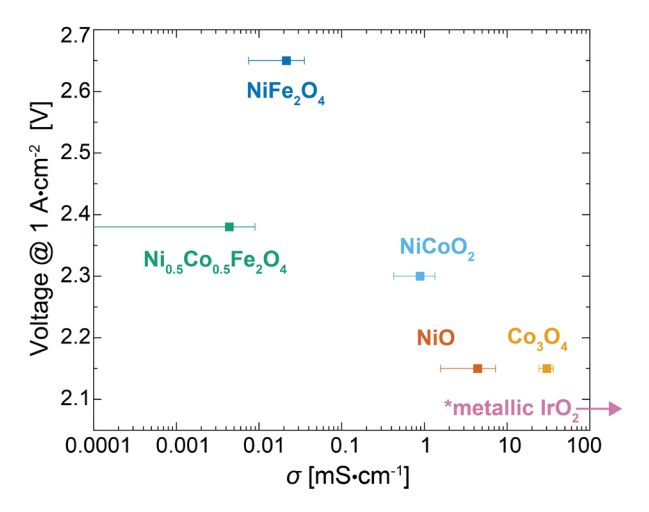


**Figure 2: Electrical conductivity of non-PGM catalysts.** Conductivity was measured by compressing the powders into a pellet (23,000 psi) and measuring electrical resistance while under compression from the slope of a polarization curve. The resistance measured for IrO<sub>2</sub> pellet was comparable to the contact/wire resistance,

and thus  $IrO_2$  is simply labeled as metallic (Figure S9). Sample size n = 3; data presented as mean  $\pm$  one standard deviation.

The conductivity of the anode layer has significant impact on AEMWE performance. <sup>[26]</sup> The electrical conductivity of each catalyst was measured by pressing each catalyst powder between two stainless steel disks under 23,000 psi and collecting a polarization curve. Catalyst performance at 1 A·cm<sup>-2</sup> follows electrical conductivity (Figure 2), indicating that the worst-performing catalysts suffer from limited available active sites due to a poor electron transport through the catalyst layer. A similar experiment was conducted with all Co-based anode catalysts measuring electronic conductivity in a catalyst/ionomer layer as opposed to pressed powders and a similar trend was observed (Figure S10 and Supplemental Methods). The ionomer environment, in combination with low-conductivity catalyst, may impede the conversion of the Ni-Fe-oxide catalysts into the more active (oxy)hydroxide form that is more conductive and would ensure better electrical conductivity between the catalyst particles and the GDL.

Several important points are evident from these data. *i)* IrO<sub>2</sub> and Co<sub>3</sub>O<sub>4</sub>, the most electronically-conductive of the catalysts tested, have superior performance in the pure-water-fed system, *ii)* the least-conductive, Fe-based catalysts, which have superior alkaline OER kinetics after restructuring to oxyhydroxides, [16, 18] perform the worst, and *iii)* mixed-metal and Fecontaining catalysts show significantly worse stability than single-metal, non-Fe-based catalysts.

Many processes could be contributing to these observed performance and durability trends. The ionomer in the catalyst layer might be degrading, for example undergoing oxidation via direct contact with the catalyst surface and thus OER intermediates. The extent of this degradation would likely vary based on catalyst properties, such as electronic conductivity and surface chemistry. The catalysts are also likely restructuring during oxidation, affecting the catalyst/ionomer interface or

leaching metals causing the loss of active sites and voids in the catalyst layer or at the catalyst/ionomer interface. Dynamic metal sites, for example soluble Fe species dissolved from the GDL or catalyst layer, might leach into the system where they could redeposit to block catalyst active sites, block OH<sup>-</sup> transport to the anode, be transported further into the MEA and decrease bulk membrane OH<sup>-</sup> conductivity, or cross fully to the cathode where they could deposit or block ion transport. Each of these possible degradation mechanisms was investigated

# 2.2. Ionomer degradation by the catalyst surface

To investigate damage occurring to the ionomer in the anode catalyst layer, the compressed AEMWE cells were disassembled and the anode GDLs analyzed with x-ray photoelectron spectroscopy (XPS). Upon disassembly the solid membrane was pulled away from the GDL exposing the leftover catalyst powder embedded in the ionomer directly in contact with the catalyst. These post-operation GDLs were soaked in 3.0 M NaCl to ion-exchange OH<sup>-</sup> for Cl<sup>-</sup> to avoid further degradation post-operation from OH<sup>-</sup> whose nucleophilicity increases with drying.

Previous studies have shown that the ionomer binder directly in contact with the catalyst layer oxidizes under operating potentials at the anode with IrO<sub>2</sub>. <sup>[13, 27]</sup> However, the mechanism by which this oxidation occurs is poorly understood. <sup>[13, 28, 29]</sup> Oxidation could be occurring directly at the catalyst/ionomer surface or chemically through reactivity with OER intermediates or other reactive oxygen species formed, for example, through radical reactivity. <sup>[30, 31]</sup> These degradation phenomena may or may not depend on catalyst type. Others have suggested that degradation rates correlate with ionomer/catalyst interaction strength, <sup>[32]</sup> and the adsorption energies of ionomer functional groups to the catalyst surface are expected to vary for different oxide catalysts. If degradation is occurring by chemical reactivity with OER intermediates, degradation may depend on catalyst activity and OER mechanism. Furthermore, AEM ionomers will oxidize at sufficiently

high voltage regardless of catalyst/electrode surface, [27] thus degradation may only depend on device operating voltage.

The extent of the ionomer oxidation by the six catalysts was assessed by XPS. The chemical structure of the ionomer and membrane used is in Figure 3a. The C 1s, N 1s, and F 1s spectra were collected on the pristine catalyst/ionomer ink and port-mortem GDLs after 20 h of operating at 500 mA·cm<sup>-2</sup> (Figure 3b). The changes to the shape and binding energy of the peaks are indicative of oxidative changes under applied potential and, in some cases, dissolution. Despite similar performance, IrO<sub>2</sub> and Co<sub>3</sub>O<sub>4</sub> appear to interact with the surrounding ionomer differently. During operation with Co<sub>3</sub>O<sub>4</sub> at the anode, the XP spectra of the ionomer does not change substantially. The N 1s peak that represents the charge-carrying groups in PiperION retains its position and shape. The XP spectra of the ionomer interacting with IrO<sub>2</sub>, on the other hand, undergoes significant chemical changes. A new high-binding-energy peak emerges at 288.4 eV after 20 h of operation and the N 1s peak vanishes. The F 1s peak also diminishes.

As 20 h is a short durability test and thus one Co<sub>3</sub>O<sub>4</sub> device was further operated for 250 h (Figure 4). The performance is similar to what has been previously observed for IrO<sub>2</sub> with both MEA's stabilizing to degradation rates < 1 mV·h<sup>-1</sup> after 150 h. <sup>[13]</sup> The C 1s region shows significant changes, comparable to that of IrO<sub>2</sub> after a long-term operation. <sup>[13]</sup> We also analyzed a separate MEA operated for 57 h (Figure S11), which showed slightly less oxidative damage.

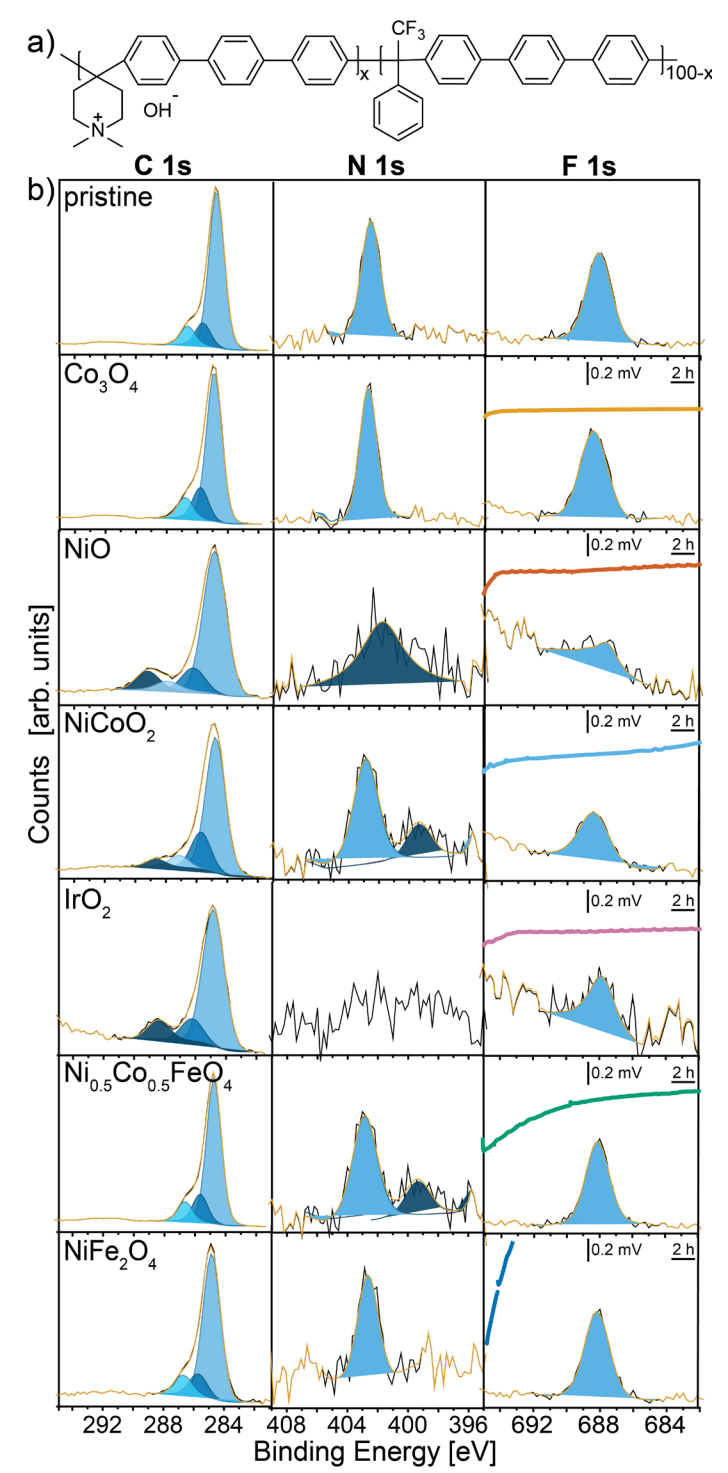


**Figure 3. Catalyst-dependent ionomer degradation.** a) Chemical structure of the membrane/ionomer used in this study (PiperION by Versogen, PAP-TP-85); b) XP spectra of C 1s, N 1s, and F 1s peaks collected on the pristine anode GDLs with the catalyst inks sprayed on (top) and the post-mortem GDLs after 20 h of operating at 500 mA·cm<sup>-2</sup> in pure water for a representative device with each catalyst type. Durability data from Figure 1c is overlaid on the F 1s spectra for reference.

The variability in ionomer oxidation rates between Co<sub>3</sub>O<sub>4</sub> and IrO<sub>2</sub> at short time scales may be explained by the difference in the catalysts' electronic conductivity. Catalyst surfaces are known to facilitate ionomer degradation, either through the polymer interactions with OER intermediates or by direct oxidation through functional groups adsorbing onto the catalyst surface.

[31-33] A more electrically-conductive catalyst could oxidize the bulk of the ionomer faster due to lower ohmic voltage losses through the percolative electronic transport pathways in the catalyst, while a less-conductive catalysts might only be able to oxidize the ionomer closer to the GDL where electronic ohmic losses are small and high oxidizing potentials remain available.

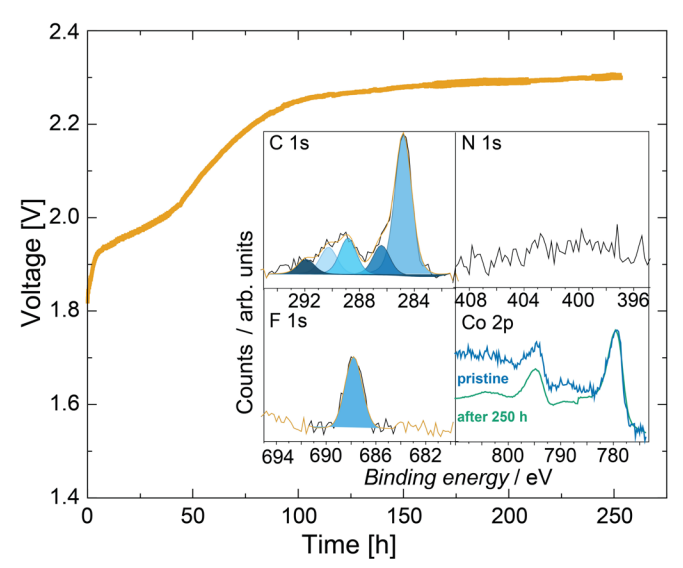


Figure 4. Extended durability testing of AEMWE with  $Co_3O_4$  anode catalyst. Cell was operated for 250 h at 500 mA·cm<sup>-2</sup> in pure water at 57 °C. A Pt-black catalyst on Toray carbon paper was used as the cathode. Inset shows XP spectra of  $Co_3O_4$  nanopowder on the pristine anode and after operation. Top panel shows XPS of ionomer (C 1s, N 1s, and F 1s) of a separate cell operated for 57 h; bottom panel shows XPS of ionomer after 250 h of operation illustrating severe oxidative damage. Sample size n = 1; a control MEA operated for 57 h is included in Figure S11.

The next two most-stable catalysts, NiO and NiCoO<sub>2</sub>, also facilitate ionomer degradation: new high-energy peaks appear in the C 1s spectra; N 1s shifts in energy and diminishes; F 1s also decreases in intensity (Figure 3b). This could be attributed to the ionomer degradation due to the

higher operating voltage, but the XPS of the two worst-performing catalysts, NiFe<sub>2</sub>O<sub>4</sub> and Ni<sub>0.5</sub>Co<sub>0.5</sub>Fe<sub>2</sub>O<sub>4</sub>, showed less changes to the ionomer structure than for NiO and NiCoO<sub>2</sub> despite operating at a higher cell voltage (Figure 3b). Changes are only observed in the N 1s peaks suggesting the ionomer dissolution or changes to the chemical structure of the charge-carrying groups. But these changes are small compared to what is observed with the better performing catalysts like IrO<sub>2</sub> or NiO. The XPS analysis of the GDLs is performed on multiple spots to obtain an averaged picture of the ionomer structure. The NiFe<sub>2</sub>O<sub>4</sub> GDL showed minor changes to the carbon peak in some of the analyzed spots, but most of the spectra showed no change.

These trends may also be explained by the differences in catalyst conductivity. For catalysts with poor electrical conductivity, only the sites near the electronically conductive GDL are active also the only region available for ionomer oxidation. XPS is surface-sensitive and will not detect degraded polymer in direct contact with the GDL if it is covered by a layer of an undegraded ionomer. It is difficult to determine the thickness of catalyst layer being analyzed during XPS. Thus, it might appear that a catalyst does not cause ionomer degradation after the 20 h run when degradation is prevalent directly next to the GDL but not on ionomer closer to the membrane.

Ionomer oxidation, however, may not be the primary degradation pathway for the Febased catalysts. To test this, the NiFe<sub>2</sub>O<sub>4</sub> catalyst was operated at a constant voltage rather than current. Even when held at 1.8 V, lower than the operating voltage of the best-performing catalyst, the activity of the system degraded rapidly, passing only a few mA of current by the end of the 20 h operation (Figure S12). The C 1s and N 1s spectra of the ionomer in contact with the catalyst show small changes compared to the pristine material (inset in Figure S12). These data suggested to us that changes in the catalyst structure and interface with the ionomer must also be considered.

## 2.3. Catalyst restructuring and leaching

Non-PGM OER catalysts are known to structurally evolve under operating conditions. <sup>[16, 17]</sup> Co, Ni, and Fe oxides, for example, oxidize during OER typically converting to more-active and electrically conductive layered oxyhydroxides. <sup>[18]</sup> These catalysts also have dynamic Fe sites that dissolve and re-deposit that are responsible for the superior OER activity. <sup>[34, 35]</sup> For Ni-Fe and Co-Fe oxyhydroxide catalysts, leaching of the metals has been reported. <sup>[34]</sup> Fe was measured to dissolve at higher rates than Ni or Co in Fe/Ni and Fe/Co oxides/oxyhydroxides, with Ni dissolution being the slowest. <sup>[34]</sup> These catalysts may also uptake additional ions present in trace amounts in electrolyte.

To assess restructuring and leaching in the mixed-metal non-PGM catalyst powders during electrolysis, we measured the metal ratios before and after operation (Figure 5a). The ratios determined by XPS are reflective of the surface composition and do not correspond to the overall composition of the nanopowders. For NiCoO<sub>2</sub>, the initial surface ratio of Co/Ni found by XPS was  $0.24 \pm 0.02$ . This ratio decreased to  $0.15 \pm 0.03$  after operation, suggesting that the catalyst is restructuring and/or leaching, forming a Ni-rich surface. The Fe/Ni ratio in NiFe<sub>2</sub>O<sub>4</sub> increased from the initial  $0.54 \pm 0.02$  to  $1.1 \pm 0.1$  indicating the formation of an Fe-rich top layer. This is likely due to Fe leaching, followed by redeposition on the surface of the catalyst (soluble Fe species are anionic in base, thus prevented from crossing to the cathode by the ohmic drop across the membrane). The Fe/Ni ratio in Ni<sub>0.5</sub>Co<sub>0.5</sub>Fe<sub>2</sub>O<sub>4</sub>, however, showed the opposite trend, decreasing from  $2.9 \pm 0.1$  to  $1.8 \pm 0.1$ , but this change was accompanied by a decrease in the Co/Ni ratio (1.0  $\pm 0.1$  to  $0.52 \pm 0.04$ ) suggesting the formation of a Ni-rich surface. Such composition on the surface is likely the result of Ni restructuring and covering Co and Fe. Co is known to be stable during OER [35, 36] and thus Co leaching is unlikely (discussed more below).

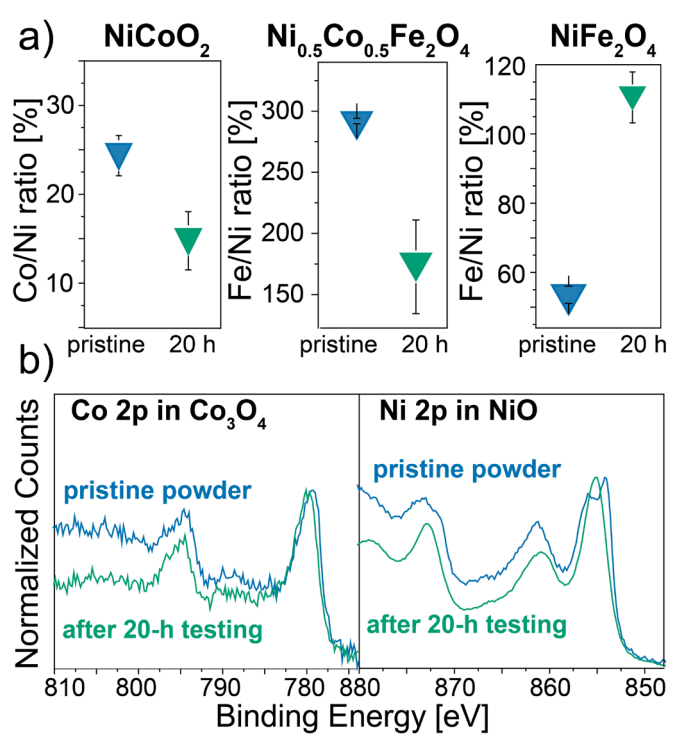


Figure 5. Comparison of non-PGM catalyst structure pre- and post-operation. a) The change in metal ratios of mixed-metal catalysts determined by XPS. Sample size n = 3; data presented as mean  $\pm$  one standard deviation. b) XPS spectra of Co 2p in Co<sub>3</sub>O<sub>4</sub> and Ni 2p in NiO. All catalysts were operated for 20 h of at 500 mA·cm<sup>-2</sup>.

For the monometallic oxides (NiO and Co<sub>3</sub>O<sub>4</sub>), we studied changes in the shape and energy of the metal XPS peaks (Figure 5b). The Co 2p peak remained unchanged after 20 h of electrolysis. The shape of the peak is consistent with Co<sub>3</sub>O<sub>4</sub>. [37] Co<sub>3</sub>O<sub>4</sub> is known to form a sub-nanometer amorphous shell during OER, otherwise maintaining crystallinity, [38, 39] and a small extent of oxidation may be occurring that is not detected by XPS. The Ni 2p peak shifted to higher binding energy and changed its shape consistent with the transition from NiO to NiOOH. [37] Ni(OH)<sub>2</sub> significantly restructures under OER conditions compared to Co(OH)<sub>2</sub> which tends to maintain its initial morphology. [36, 40] The change in oxidation state and structure might be accompanied by Ni<sup>2+/3+</sup> leaching/redeposition. The changes to the catalyst structure likely explain the observed degradation behavior. Catalyst/ionomer interactions influence electrolyzer performance and

durability. <sup>[33, 41, 42]</sup> Structural evolution and cation leaching/redeposition likely disrupts the catalyst/ionomer interfaces. For example, as NiO dynamically restructures to form more disordered NiOOH, the physical proximity of the ionomer and catalyst likely decreases, increasing *iR* and/or decreasing ionic conductivity, leading to higher voltages without observing significant ionomer oxidation by XPS. Leaching of the metal cations and their consequent redeposition on the electrode surface could further disrupt the catalyst/ionomer network. The lack of restructuring and leaching/redeposition under OER conditions likely contributes to the better durability of Co<sub>3</sub>O<sub>4</sub>.

# 2.4. The role of dynamic Fe species

Leached ions also can participate in chemical reactions with the ionomer leading to chemical changes (e.g. Fenton-type oxidation reactions). [43, 44] Fe is particularly dynamic, and thus the role of soluble Fe ions was further investigated. As we observed the formation of a Fe-rich surface on the GDL tested with NiFe<sub>2</sub>O<sub>4</sub>, we focused on that catalyst to pinpoint the role the Fe ions play in electrolyzer performance. We hypothesized that Fe leaches and redeposits onto the anode during operation forming an amorphous blocking layer that is disruptive to the catalyst/ionomer network decreasing ionic conductivity.

To probe the role of soluble Fe species, we intentionally added soluble Fe to the water feed. An MEA with a Co<sub>3</sub>O<sub>4</sub> anode was operated for ~ 10 h to stabilize, then 1 ppm Fe<sup>3+</sup> was flowed to the anode while pure water was maintained at the cathode from a separate pump and water reservoir (Figure 6). The Fe increased the degradation rate to ~4 mV h<sup>-1</sup>. The run was carried out for 40 h, during which the degradation continued at this constant rate. XPS shows large changes to the C 1s and N 1s spectra. The performance of Co<sub>3</sub>O<sub>4</sub> tested for 40 h in the absence of Fe (Figure 6, gold) did not degrade as rapidly. However, the XPS analysis of the ionomer at the anode after the 40-h Fe-free run shows nearly identical changes to the C 1s and N 1s peaks (Figure 6 inset).

As discussed above, Co<sub>3</sub>O<sub>4</sub> alone oxidizes the ionomer but at a slower rate compared to IrO<sub>2</sub> (Figure 4). One might attribute this new degradation to soluble Fe species crossing the AEM to the cathode where it could block active sites on Pt or otherwise facilitate cathodic degradation, but Fe was not detected on the cathode GDL post-operation by XPS (Figure S13). Thus, it appears the introduction of Fe is accelerating the degradation in the anode. Soluble Fe ions likely deposit on or adsorb to the anode catalyst surface disrupting the ionic conductivity of the catalyst/ionomer network. To investigate the role of soluble metal ions, the Co<sub>3</sub>O<sub>4</sub> and Ni<sub>0.5</sub>Co<sub>0.5</sub>Fe<sub>2</sub>O<sub>4</sub> anode systems were operated in pure water and the anode effluent water was analyzed with ICP-MS. The Fe, Ni, and Co concentrations measured for both systems were less than 5 ppb and no significant dissolution was observed (Figure S14). It is likely the catalyst surfaces, particularly those with Ni and Fe, are dynamic at the local interface – dissolving to form voids and redepositing in unwanted locations – and that metal ions are not washed out into the system in the absence of soluble electrolyte to facilitate formation of stable dissolution products.

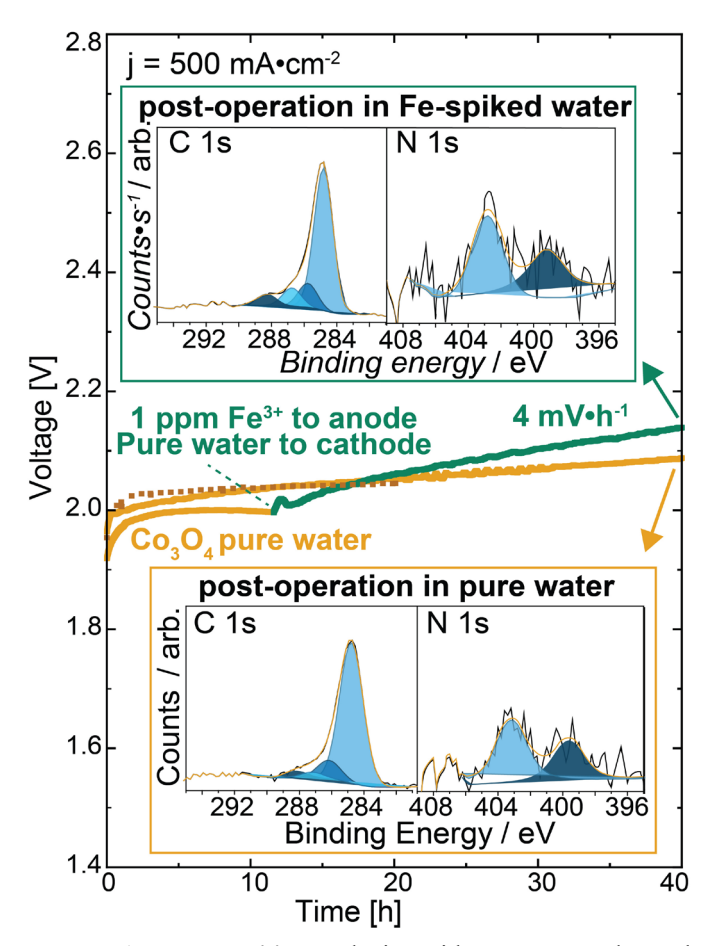


**Figure 6. Effect of soluble Fe on AEM durability.** A device with a Co<sub>3</sub>O<sub>4</sub> anode catalyst was operated in pure water until stabilizing (yellow), after which the anode inlet was moved to a solution of 1 ppm Fe<sup>3+</sup> (green trace). The 20 h Co<sub>3</sub>O<sub>4</sub> run is shown in darker yellow dashed line for reference. Inset: XP spectra of the anode GDL post-Fe spike (top) and pure water (bottom) operation.

## 3. Conclusion

We discovered critical catalyst processes that affect the performance and stability of AEMWE devices key for scalable H<sub>2</sub> production (summarized in Figure 7). The experiments indicate that conductive IrO<sub>2</sub> provides more active sites to oxidize ionomer, as opposed to mixed Ni/Fe/Co catalysts that show a lower extent of oxidation by XPS likely due to much lower electrical conductivity. IrO<sub>2</sub> is sufficiently conductive, so any Ir sites in contact with the ionomer network

are active, leading to rapid ionomer degradation throughout the catalyst layer. Co<sub>3</sub>O<sub>4</sub>, while less electrically conductive, appears conductive enough to maintain sufficient activity throughout the catalyst layer. Improved performance is likely possible by further improving the electrical properties. The OER on Co<sub>3</sub>O<sub>4</sub> likely converts the particle surface to CoOOH, but the depth of conversion is sufficiently thin as to not disrupt the catalyst/ionomer interface. The ionomer still oxidatively degrades throughout the catalyst layer but at a slower rate than for IrO<sub>2</sub>. XPS shows NiO converts to nominally NiOOH, and our evidence suggests that changes to ionomer/catalyst interface associated with this transition contribute to faster degradation. The low electronic conductivity of NiCoO<sub>2</sub>, Ni<sub>0.5</sub>Co<sub>0.5</sub>Fe<sub>2</sub>O<sub>4</sub>, and NiFe<sub>2</sub>O<sub>4</sub> confines OER to the region in direct contact with the stainless-steel GDL support. As the ionomer oxidizes, ionic conductivity to this region decreases. Ionically accessible catalyst sites are now further from the GDL, but low electronic conductivity limits reactivity of these sites creating a resistive layer and cell voltage increases. This ionomer degradation would not necessarily be observed by XPS as it is a surface-sensitive technique, and the degradation does not extend into the bulk of the catalyst layer.

NiCoO<sub>2</sub> and Ni<sub>0.5</sub>Co<sub>0.5</sub>Fe<sub>2</sub>O<sub>4</sub> show a Ni-rich surface after operation and NiFe<sub>2</sub>O<sub>4</sub> shows an Ferich surface after operation. Changes to the ionomer/catalyst interface associated with this rearrangement likely result in changes to surface contact and charge-transfer resistance. For NiCoO<sub>2</sub>, as CoO<sub>x</sub> is known to be stable during operation, <sup>[35, 36]</sup> we hypothesize Ni ions are leaching/redepositing from the catalyst, possibly due to a lower local-pH environment created by the reduced OH<sup>-</sup> conductivity to the region. The Fe-rich surface for NiFe<sub>2</sub>O<sub>4</sub> is likely due to dominant Fe leaching/redeposition. For Ni<sub>0.5</sub>Co<sub>0.5</sub>Fe<sub>2</sub>O<sub>4</sub> both Ni and Fe are likely leaching. Leached ions can create voids in the ionomer network disrupting the ionic connectivity and physical coupling between ionomer and catalysts. Ions that redeposit on the catalyst likely change

ionomer/catalyst interactions, reducing ionic conductivity and/or blocking active sites. In solution, those ions may also accelerate existing, or introduce additional, ionomer degradation mechanisms. Multiple degradation modes are likely occurring simultaneously with the Ni-Fe-oxides contributing to their rapid failure during device operation.

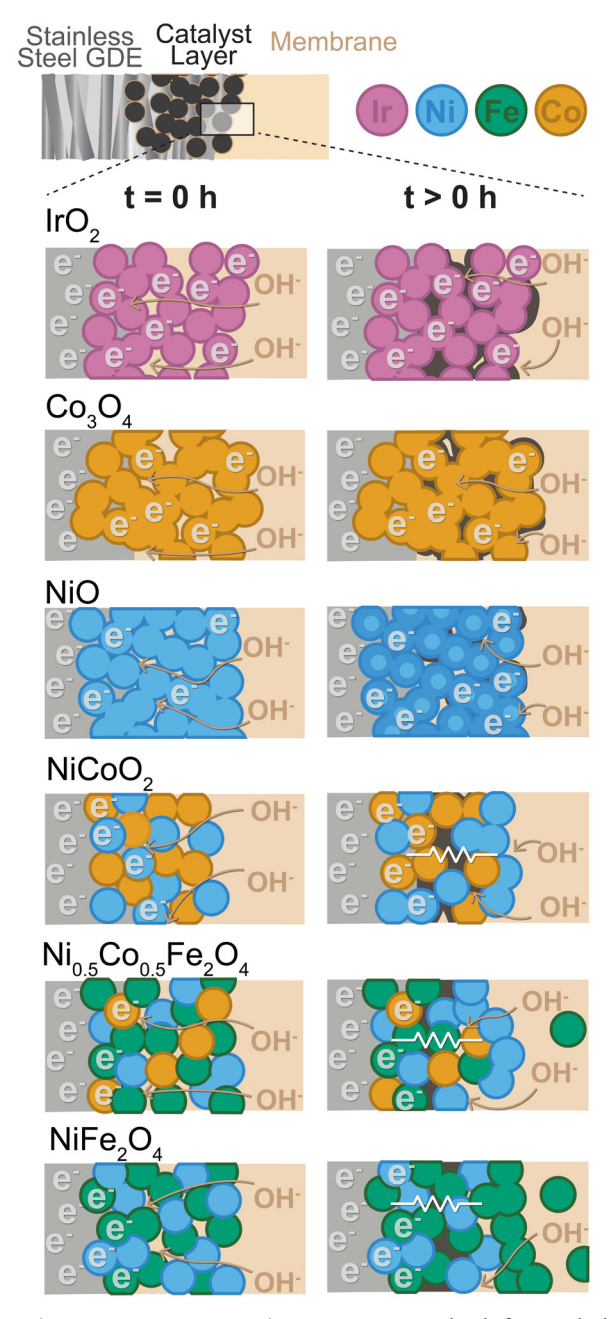


**Figure 7**. **Summary of possible anode degradation processes.** The left panel shows the catalyst starting state and right after extended operation. Pristine ionomer is shown in tan; degraded ionomer regions are dark

brown. IrO<sub>2</sub> (pink) degrades the ionomer throughout the catalyst layer but has sufficient electronic conductivity to still access ionically conductive regions. Co<sub>3</sub>O<sub>4</sub> (gold) also degrades the ionomer but at a slower rate and has sufficient electrical conductivity to maintain some activity throughout the catalyst layer. NiO (light blue) converts to the electrically conductive NiOOH phase (dark blue), increasing electronic conductivity but disrupting the catalyst/ionomer interaction. NiCoO<sub>2</sub> (blue and gold), Ni<sub>0.5</sub>Co<sub>0.5</sub>Fe<sub>2</sub>O<sub>4</sub> (blue, gold, and green), and NiFe<sub>2</sub>O<sub>4</sub> (blue and green) have low electronic conductivity. Ionomer degradation decreases ionic pathways to the catalyst creating a resistive zone. NiCoO<sub>2</sub> and Ni<sub>0.5</sub>Co<sub>0.5</sub>Fe<sub>2</sub>O<sub>4</sub> show a Nirich surface after operation and NiFe<sub>2</sub>O<sub>4</sub> shows an Fe-rich surface after operation, both likely due to dissolution/redeposition.

Understanding the behavior of non-PGM catalysts in industry relevant (nominally) pure-water-fed AEMWE devices is critical to inform design for advanced electrolyzer technology. Here, we isolate anode catalyst processes from overall device performance and report the first chemical insight into catalyst characteristics and processes driving system degradation. Analyzing the performance and stability of five non-PGM anode catalysts in comparison with a baseline IrO2 catalyst in a pure-water-fed AEM electrolyzer, we reveal that high electronic conductivity of the catalyst results in a better voltage performance but faster ionomer oxidation. We also discover a variety of degradation processes occurring for each catalyst. The main sources of degradation stem from catalyst restructuring and ionomer oxidation under OER-relevant conditions—the structural stability of IrO2 and Co<sub>3</sub>O<sub>4</sub>, coupled with good electrical conductivity and OER activity, are the reasons for their superior durability. We have thus begun to isolate ionomer degradation from catalyst phenomena during operation in an MEA configuration and simultaneously provided fundamental insight into non-PGM catalyst operation in industry relevant configurations and conditions. Our approach also uses a simple, scalable GDL preparation method and commercially

available catalyst to show Co<sub>3</sub>O<sub>4</sub> is a viable option for developing non-PGM-based AEM electrolyzers, which is important for AEMWE to grow into a competitive future technology.

## 4. Experimental Section

Catalyst Dispersions and GDL Coating. Pt black (high surface area, Fuel Cell Store) nanoparticles were used as the cathode catalyst for all trials. Co<sub>3</sub>O<sub>4</sub> (99.5%, 30-50nm), NiO (99.5%, 15-35 nm), NiCoO<sub>2</sub> (99.9%, 20 nm), NiFe<sub>2</sub>O<sub>4</sub> (99.99%, 20 nm), Ni<sub>0.5</sub>Co<sub>0.5</sub>Fe<sub>2</sub>O<sub>4</sub> (99.995%, 40 nm, US Research Nanomaterials), and IrO<sub>2</sub> (core/shell Ir/IrO<sub>x</sub>, Fuel Cell Store) nanoparticles were used at the anode. Cathode and anode electrodes were prepared identically by spray-coating using a published method. <sup>[13]</sup> Catalyst inks were prepared by mixing the catalyst powder (100 mg), water (0.5 g), isopropyl alcohol (1.7 g), and 5 wt. % TP-85 (Versogen) ionomer (200 mg). Catalyst inks were sonicated for 1 h to disperse before spray coating using an airbrush (Testors, Aztek A2203). Pt black was sprayed onto carbon paper (Toray 090, Fuel Cell Store) and anode catalysts were sprayed onto a woven stainless-steel mesh (25AL3, Bekaert). A catalyst loading between 2.2 and 2.5 mg·cm<sup>-2</sup> was determined by mass difference. A thin layer of ionomer (2-5 wt. %) was then sprayed on top of the electrode. This resulting percentage is the lowest mass/thinnest ionomer layer that can be applied with uniform thickness.

Membrane Conditioning. PAP-TP-85 membranes (40  $\mu$ m, Versogen) were conditioned according to manufacturer instructions. The membranes were soaked in 0.5 M KOH for 24 h, replacing the solution with fresh KOH after 1 h. Membranes were stored in 0.5 M KOH when not in use.

MEA Assembly and Hardware Operation. GDLs were cut to 1 cm<sup>2</sup> and assembled in the electrolyzer according to published procedures. [13] A water tank filled with 18.2 M $\Omega$ ·cm provided

water to the cathode and anode at  $125 \text{ mL} \cdot \text{min}^{-1}$ . [13] The anode water flow was recirculated in the system while the cathode water flow was degassed in a chemical hood then recirculated back into the water tank. The temperature of the water source was set to 60 °C. The temperature in the electrolyzer cell at this temperature equilibrated to  $57 \pm 1$  °C and was monitored with a thermocouple inserted into the anode and cathode cell hardware plates. The temperature difference between anode and cathode was maintained to less than  $\pm 1 \text{ C}^{\circ}$ .

Applied Current Testing Conditions. All electrochemical testing was conducted using a potentiostat (BioLogic VSP-300) equipped with a 10A/5V booster cable. All tests were conducted under chronopotentiometric conditions unless otherwise indicated. The MEA was conditioned by stepping the current from 100 mA·cm<sup>-2</sup> to 1 A·cm<sup>-2</sup> in 100 mA intervals, holding for 2 min at each step. Impedance spectra were then collected from 500 kHz to 200 mHz at 50 mA·cm<sup>-2</sup>. Then, the cell was held at 1 V to observe the steady-state electrolysis current decay to zero, confirming there were no pinholes or shunt pathways present. The cell was brought back to 1 A·cm<sup>-2</sup> for 2 min to stabilize. The potential was then recorded, and the current was decreased in 100 mA·cm<sup>-2</sup> steps until reaching 100 mA·cm<sup>-2</sup>, further decreased to 50 mA·cm<sup>-2</sup>, and lastly 10  $\text{mA} \cdot \text{cm}^{-2}$ , measuring the potential for 10 s at each step to collect the J-V curve. The cell was held at 500 mA·cm<sup>-2</sup> for stability measurements. During 20 h stability testing, impedance data, as described above, was collected after 1 h, 3 h, 8 h, and 20 h. For the 40 h and 200 h tests, impedance was collected only at the start and end of durability testing. After analysis, the cells were disassembled, and the ionomer and membrane were converted to the Cl<sup>-</sup> counter anion form by submerging the MEA in 3 M NaCl solution for at least 30 min (to prevent OH- attack induced by drying the ionomer). The materials were then rinsed thoroughly with 18.2 M $\Omega$ ·cm water for 30 s and dried in air.

Applied Voltage Testing Conditions. To test the performance of NiFe<sub>2</sub>O<sub>4</sub> at a lower voltage, the cell was tested under galvanostatic conditions. For this, the MEA was conditioned by stepping the voltage from 1.7 to 1.9 V in 50 mV steps. Impedance spectra were collected over the same frequency range at 1.6 V. The cell was then stepped down from 1.9 to 1.6 V in 50 mV steps held at 10 s to record the *J-V* curve. Durability testing was conducted at 1.8 V. Impedance data of the same conditions was collected at the same time points as the chronopotentiometric testing for consistency. The MEA was disassembled and converted to Cl<sup>-</sup> counter ion as described above.

Fe Spike Test. An MEA with a Co<sub>3</sub>O<sub>4</sub> anode was prepared and conditioned according to the above procedure, but water was flowed to the anode and cathode with separate water pumps. The anode was flowed at 75 mL·min<sup>-1</sup> and the cathode 75 mL·min<sup>-1</sup>, which was the highest flow rate possible before high back pressure caused the water line to detach from the pump. Durability testing was operated at 500 mA·cm<sup>-2</sup>. When the degradation rate stabilized to below 1 mV·h<sup>-1</sup>, the inlet line for the anode pump was moved to a 1 ppm Fe<sup>3+</sup> solution composed of 0.19 mM Fe(NO<sub>3</sub>)<sub>3</sub>·9H<sub>2</sub>O (ACS reagent grade ≥98%, Sigma). The solution was held at the same temperature as the water tank to maintain a constant hardware temperature. Current was held at 500 mA·cm<sup>-2</sup> during this time and durability testing was continued for an additional 28 h. The MEA was disassembled and converted to Cl<sup>-</sup> counter ion as described above.

Catalyst Conductivity Measurements. The catalyst powders (~200 mg) were pressed between two stainless steel disks inset in a plastic holder (Figure S7). An aluminum bar was placed above and below the disks to make electric contact, which were connected to a potentiostat using copper wire. Plastic sheets were placed above and below the aluminum to prevent short-circuit through the metal press. The powders were compressed to 23,000 psi. The thickness of the powder was measured by measuring the distance between the top and bottom of the steel disks using a

digital micrometer and subtracting the thickness of the disks with no catalyst powder. Polarization curves were collected from -1 to 1 V at 1 V·s<sup>-1</sup> (Figure S8). The contact resistance was measured by the same method with no catalyst between the two disks. For the blank and IrO<sub>2</sub> measurements the range was adjusted to -0.02 to 0.02 V at 10 mV·s<sup>-1</sup> to prevent current overload (Figure S9). The measurement for IrO<sub>2</sub> matched that of the contact resistance, and thus a value is not reported for this catalyst. For all other catalysts the resistance was obtained from a linear fit of the obtained current-voltage curve. The lead resistance was subtracted before calculating conductivity according to  $\sigma = l/(RA)$ , where  $\sigma$  is electrical conductivity in S·cm<sup>-1</sup>, l is the thickness of the catalyst powder in cm, R is the measured resistance in  $\Omega$ , and A is the disk surface area in cm<sup>2</sup>.

Catalyst Surface Area Measurements. N<sub>2</sub> adsorption/desorption isotherms were measured using a Micromeritics ASAP 2020 surface area analyzer at 77 K. Specific surface areas (S<sub>BET</sub>) of the samples were calculated using the Brunauer-Emmett-Teller (BET) method, and pore widths and pore volumes (V<sub>p</sub>) were calculated using the Barrett, Joyner, and Halenda (BJH) adsorption curves. Samples were suspended in isopropyl alcohol and dried at room temperature under vacuum for 12 h. Samples were then activated at 393 K (Co<sub>3</sub>O<sub>4</sub>, NiFe<sub>2</sub>O<sub>4</sub>, Ni<sub>0.5</sub>Co<sub>0.5</sub>Fe<sub>2</sub>O<sub>4</sub>, NiCoO<sub>2</sub>, and IrO<sub>2</sub>) or 423 K (NiO) for at least 24 h to remove the solvent and trapped gas. Activation was considered complete when the outgassing rate fell below 2.5 μtorr·min<sup>-1</sup>. The sample mass was calculated by the difference in mass between the empty sample tube and the loaded sample tube post-activation. The sample tube was massed before and after analysis to ensure the sample mass was unchanged during analysis.

1Catalyst Testing on Quartz-Crystal-Microbalance (QCM) Electrodes in KOH. The catalyst inks were prepared identical to device testing and were spin-coated onto 5 MHz Au/Ti quartz crystals (Fil-Tech) at 3000 rpm and dried at 80 °C to obtain the loading of ~ 22 μgMo·cm<sup>-2</sup> (normalized to

exclude the mass of the ionomer). The cyclic voltammetry (CV) plots were collected using a potentiostat (BioLogic, SP-200) in 1.0 M KOH with the working electrodes connected to the QCM controller (Stanford Research Systems QCM200). Potentials in three-electrode modes were measured versus a 1 M KOH Hg/HgO reference electrode (CH Instruments). The reference electrode was calibrated before the electrochemical measurements using a reversible hydrogen electrode (HydroFlex).

During the three-electrode QCM experiments the electrolytes were either bubbled with high-purity  $N_2$  (Figure 1d) or conducted in open air (Figure S6 and S6). All three-electrode electrochemical data were corrected for uncompensated series resistance ( $R_u$ ), which was determined by equating  $R_u$  to the minimum total impedance in the frequency regime between 10 and 50 kHz, where the capacitive and inductive impedances are negligible, and the phase angle was near zero.

XPS Analysis of Pristine and Post-Mortem GDLs. XPS measurements were performed on an ESCALAB 250 (ThermoScientific) using Al Kα monochromated (20 eV pass energy, 500 μm spot size) and non-monochromated Mg Kα (400 W, 75 eV pass energy) flood sources. The use of the Mg source is critical in discerning Fe in the samples as typical Al sources exhibit overlap of the Fe 2p peaks with Ni and Co Auger LMM features. The samples were charge-neutralized via an in-lens electron source. Spectra were analyzed with ThermoScientific Avantage 5.99 software. The binding energies were calibrated to the C 1s signal at 284.8 eV.

The catalyst powders that do not contain Fe were analyzed as sprayed inks on stainless-steel GDLs prior and after the AEMWE operation with the ionomer ion-exchanged to Cl<sup>-</sup> form. To avoid signal contribution from the Fe-rich stainless-steel, the metal ratios in the Fe-containing catalysts were analyzed separately from GDLs. To obtain the metal ratios in pristine catalysts, the

powders were analyzed on a piece of carbon tape. To assess the changes to the metal ratios after electrolysis, the GDLs were sonicated in ethanol to remove the catalyst layer. The lose powder was collected, dried, and analyzed on a piece of carbon tape. The C 1s, N 1s, and F 1s spectra for Fe-containing catalysts were obtained with the inks on GDLs similarly to the other catalysts.

Statistical Analysis. For all data reported, no outliers were eliminated. Figure 1a and S3: sample size n = 3; data is reported as mean  $\pm$  one standard deviation. Figure 1b: Sample size n =1. All raw data is shown in points. Data was fit to the adapted Randle's Circuit shown using the zfit function of EC-Lab V11.36 software. Figure 1c: Sample size n = 1 is shown for clarity with duplicate measurements shown in Figure S4. The data point collected at t = 0 was eliminated for all curves as the current had not yet reached 500 mA·cm<sup>-2</sup>. Figure 1d: Sample size n = 1 is shown for clarity with replicate averaged data shown in Figure S5. The current was normalized to BET surface area of each electrode, calculated using the catalyst loading and measured BET surface area. Figure 2: sample size n = 3; data is reported as mean  $\pm$  one standard deviation. A linear fit of the three voltage sweep cycles was obtained using the linear fit function in EC-Lab V11.36 software. Figures 3, 4, 5b, 6, and S9: Sample size n = 1; three spots on the sample were scanned to confirm all spectra were representative of the full sample, one was used for analysis and fit. Figure 5a: Sample size n = 3; data is reported as mean  $\pm$  one standard deviation. All XP spectra were analyzed and fit using Thermo Scientific Avantage 4.88 software. The C 1s signal at 284.8 eV was used to calibrate the binding energy scale. Figure S5: electrochemical data and top XPS inset sample size n = 1, bottom XPS inset sample size n = 3; data is reported as mean  $\pm$  one standard deviation. Figure S7: Sample size n = 1. Data was processed identical to Figure 2. Figure S10: n= 1; samples were analyzed using Qtegra ISDS Software. 5 replicate scans were conducted for each sample and the values are reported as mean  $\pm$  one standard deviation. Correlation coefficients

for Ni, Fe, and Co calibration curves were greater than 0.999. **Table 1:** BET surface areas sample size n = 1. Samples were analyzed using ASAP 2020 Plus 2.00. Error reported is a mean squared deviation calculated by linear regression. Correlation coefficient for BET fit was 0.999 or greater for all samples.

## **Supporting information**

Supporting Information is available from the Wiley Online Library or from the author.

#### Acknowledgements

This work was supported by the U.S. Department of Energy's Office of Energy Efficiency and Renewable Energy (EERE) under the Fuel Cell Technologies Office (FCTO) under award DE-EE0008841. The authors are grateful to K. Spence and A. Matten for preliminary catalyst testing. We thank S. Golledge for assistance with XPS. RAK and GAL contributed equally to this work and should be regarded as joint first-authors. RAK, GAL, and SWB designed the study, analyzed the data, and wrote the manuscript. RAK collected and analyzed all XPS with the support of TNS. RAK and GAL collected and analyzed three-electrode electrochemical measurements with the support of TNS and LT. GAL performed and analyzed all electrolyzer MEA and conductivity measurements with the support of SRB and WLT. DG and JG collected ICP-MS samples. LT conducted ICP-MS analysis. KF conducted gas adsorption experiments for catalyst surface area analysis. JEH provided intellectual advisement. The ICP-MS instrument was supported by NSF award #2117614 from the Major Research Instrumentation program.

#### **Conflict of Interest**

The authors declare no conflict of interest.

# **Data Availability**

The raw data for this study is available from the authors upon reasonable request.

## References

- [1] B. Pivovar, N. Rustagi, S. Satyapal, *Electrochem. Soc. Interface* **2018**, 27, 47.
- [2] G. W. Crabtree, M. S. Dresselhaus, M. V. Buchanan, *Phys Today* **2004**, 57, 39.
- [3] K. Ayers, N. Danilovic, R. Ouimet, M. Carmo, B. Pivovar, M. Bornstein, *Annu. Rev. Chem. Biomol. Eng.* **2019**, 10, 219.
- [4] K. Zeng, D. Zhang, *Prog. Energy Combust. Sci.* **2010**, 36, 307.
- [5] M. Carmo, D. L. Fritz, J. Mergel, D. Stolten, *Int. J. Hydrogen Energy* **2013**, 38, 4901.
- [6] A. Carbone, S. C. Zignani, I. Gatto, S. Trocino, A. S. Aricò, *Int. J. Hydrogen Energy* 2020, 45, 9285.
- [7] A. Y. Faid, L. Xie, A. O. Barnett, F. Seland, D. Kirk, S. Sunde, *Int. J. Hydrogen Energy*2020, 45, 28272.
- [8] P. Chen, X. Hu, Adv. Energy Mater. **2020**, 10, 2002285.
- [9] H. Koshikawa, H. Murase, T. Hayashi, K. Nakajima, H. Mashiko, S. Shiraishi, Y. Tsuji, ACS Catal. 2020, 10, 1886.
- [10] D. Li, E. J. Park, W. Zhu, Q. Shi, Y. Zhou, H. Tian, Y. Lin, A. Serov, B. Zulevi, E. D. Baca, C. Fujimoto, H. T. Chung, Y. S. Kim, *Nat. Energ.* 2020, 5, 378.
- [11] N. Hassan, Y. Zheng, P. Kohl, W. E. Mustain, *Journal of The Electrochemical Society* **2022**.

- [12] A. Kiessling, J. C. Fornaciari, G. Anderson, X. Peng, A. Gerstmayr, M. R. Gerhardt, S. McKinney, A. Serov, Y. S. Kim, B. Zulevi, A. Z. Weber, N. Danilovic, *Journal of The Electrochemical Society* **2021**, 168, 084512.
- [13] G. A. Lindquist, S. Z. Oener, R. Krivina, A. R. Motz, A. Keane, C. Capuano, K. E. Ayers,
   S. W. Boettcher, ACS Appl. Mater. Interfaces 2021, 13, 51917.
- [14] R. Soni, S. Miyanishi, H. Kuroki, T. Yamaguchi, ACS Appl. Energy Mater. 2021, 4, 1053.
- [15] D. Xu, M. B. Stevens, M. R. Cosby, S. Z. Oener, A. M. Smith, L. J. Enman, K. E. Ayers,
  C. B. Capuano, J. N. Renner, N. Danilovic, Y. Li, H. Wang, Q. Zhang, S. W. Boettcher,
  ACS Catal. 2019, 9, 7.
- [16] M. B. Stevens, L. J. Enman, E. H. Korkus, J. Zaffran, C. D. M. Trang, J. Asbury, M. G. Kast, M. C. Toroker, S. W. Boettcher, *Nano Res.* 2019, 12, 2288.
- [17] M. B. Stevens, C. D. M. Trang, L. J. Enman, J. Deng, S. W. Boettcher, J. Am. Chem. Soc.2017, 139, 11361.
- [18] L. Trotochaud, S. L. Young, J. K. Ranney, S. W. Boettcher, J. Am. Chem. Soc. 2014, 136, 6744.
- [19] L. Wang, V. A. Saveleva, M. J. Eslamibidgoli, D. Antipin, C. Bouillet, I. Biswas, A. S. Gago, S. S. Hosseiny, P. Gazdzicki, M. H. Eikerling, E. R. Savinova, K. A. Friedrich, *ACS Appl. Energy Mater.* **2022**, 5, 2221.
- [20] A. Meena, P. Thangavel, D. S. Jeong, A. N. Singh, A. Jana, H. Im, D. A. Nguyen, K. S. Kim, *Applied Catalysis B: Environmental* **2022**, 306, 121127.
- [21] B. Mayerhöfer, F. D. Speck, M. Hegelheimer, M. Bierling, D. Abbas, D. McLaughlin, S. Cherevko, S. Thiele, R. Peach, *Int. J. Hydrogen Energy* 2022, 47, 4304.

- [22] J. Xiao, A. M. Oliveira, L. Wang, Y. Zhao, T. Wang, J. Wang, B. P. Setzler, Y. Yan, ACS Catal. 2021, 11, 264.
- [23] J. Yang, M. J. Jang, X. Zeng, Y. S. Park, J. Lee, S. M. Choi, Y. Yin, *Electrochem. Commun.*2021, 131, 107118.
- [24] P. Thangavel, M. Ha, S. Kumaraguru, A. Meena, A. N. Singh, A. M. Harzandi, K. S. Kim, *Energy Environ. Sci.* **2020**, 13, 3447.
- [25] P. Thangavel, G. Kim, K. S. Kim, J. Mater. Chem. A. 2021, 9, 14043.
- [26] N. U. Hassan, M. Mandal, B. Zulevi, P. A. Kohl, W. E. Mustain, *Electrochim. Acta* 2022, 409, 140001.
- [27] R. A. Krivina, G. A. Lindquist, M. C. Yang, A. K. Cook, C. H. Hendon, A. R. Motz, C. Capuano, K. E. Ayers, J. E. Hutchison, S. W. Boettcher, *ACS Appl. Mater. Interfaces* **2022**.
- [28] D. Li, A. R. Motz, C. Bae, C. Fujimoto, G. Yang, F.-Y. Zhang, K. E. Ayers, Y. S. Kim, Energy Environ. Sci. 2021, 14, 3393.
- [29] I. Martens, L. G. A. Melo, M. M. West, D. P. Wilkinson, D. Bizzotto, A. P. Hitchcock, ACS Catal. 2020, 10, 8285.
- [30] H. B. Tao, Y. Xu, X. Huang, J. Chen, L. Pei, J. Zhang, J. G. Chen, B. Liu, *Joule* 2019, 3, 1498.
- [31] G. Hübner, E. Roduner, J. Mater. Chem. 1999, 9, 409.
- [32] J. Wang, Y. Zhao, B. P. Setzler, S. Rojas-Carbonell, C. Ben Yehuda, A. Amel, M. Page,L. Wang, K. Hu, L. Shi, S. Gottesfeld, B. Xu, Y. Yan, *Nat. Energ.* 2019, 4, 392.
- [33] S. A. Berlinger, B. D. McCloskey, A. Z. Weber, ACS Energy Lett. 2021, 6, 2275.

- [34] D. Y. Chung, P. P. Lopes, P. Farinazzo Bergamo Dias Martins, H. He, T. Kawaguchi, P. Zapol, H. You, D. Tripkovic, D. Strmcnik, Y. Zhu, S. Seifert, S. Lee, V. R. Stamenkovic, N. M. Markovic, Nat. Energ. 2020, 5, 222.
- [35] T. Zhang, M. R. Nellist, L. J. Enman, J. Xiang, S. W. Boettcher, *ChemSusChem* **2019**, 12, 2015.
- [36] C. Dette, M. R. Hurst, J. Deng, M. R. Nellist, S. W. Boettcher, *ACS Appl. Mater. Interfaces* **2019**, 11, 5590.
- [37] M. C. Biesinger, L. W. M. Lau, A. R. Gerson, R. S. C. Smart, *Phys. Chem. Chem. Phys.*2012, 14, 2434.
- [38] A. Bergmann, E. Martinez-Moreno, D. Teschner, P. Chernev, M. Gliech, J. F. de Araújo,T. Reier, H. Dau, P. Strasser, *Nat. Commun.* 2015, 6, 8625.
- [39] T. Wiegmann, I. Pacheco, F. Reikowski, J. Stettner, C. Qiu, M. Bouvier, M. Bertram, F. Faisal, O. Brummel, J. Libuda, J. Drnec, P. Allongue, F. Maroun, O. M. Magnussen, ACS Catal. 2022, 3256.
- [40] J. Deng, M. R. Nellist, M. B. Stevens, C. Dette, Y. Wang, S. W. Boettcher, *Nano Lett.*2017, 17, 6922.
- [41] R. Jinnouchi, K. Kudo, K. Kodama, N. Kitano, T. Suzuki, S. Minami, K. Shinozaki, N. Hasegawa, A. Shinohara, *Nat. Commun.* **2021**, 12, 4956.
- [42] C. Santoro, A. Lavacchi, P. Mustarelli, V. Di Noto, L. Elbaz, D. R. Dekel, F. Jaouen, *ChemSusChem*, e202200027.
- [43] G. A. Lindquist, Q. Xu, S. Z. Oener, S. W. Boettcher, *Joule* **2020**, 4, 2549.
- [44] H.-F. Lu, H.-F. Chen, C.-L. Kao, I. Chao, H.-Y. Chen, *Phys. Chem. Chem. Phys.* **2018**, 20, 22890.